The Impact of Photospheric Expansion Bursts on the Neutron Star Accretion Flow – Thesis Proposal –

Julia Speicher

1 Introduction

Neutron stars in *low-mass X-ray binaries* (LMXBs) accrete matter from a donor star. The emission of the neutron star and the accretion environment is detectable in the X-ray band (section 2.1). Due to unstable nuclear burning, neutron stars can undergo *Type I X-ray bursts* and emit vasts amount of radiation (section 2.2). Observations as well as simulations showed that this radiation impacts the accretion flow environment, both its structure as well as its emission (section 2.2.1, 3). If the burst luminosity is high enough, radiation pressure can lift off the neutron star photosphere and remove material from the neutron star (section 2.3). These *photospheric radius expansion* (PRE) bursts have been used to estimate the distance to neutron stars and to constrain their mass and radii (section 2.3.1). However, these studies often neglect the effect of the burst on the accretion environment and its potential impact on the emission. For my thesis, I therefore propose to simulate the accretion environment impacted by a PRE burst with the code *Cosmos++* (section 4).

2 Literature Review

2.1 Neutron Stars and Their Accretion Environment

Neutron stars are one of the most compact objects in the universe and are born through supernovae of massive stars (LeBlanc 2010). As they mark the end of a star's life, neutrons stars are found in regions of old star populations, such as in the halo, in globular clusters of halos, and at the galactic center (e.g., Grimm et al. 2002; Kuranov & Postnov 2006; Sartore et al. 2010).

A neutron star can form binaries with other stars. If the binary star is a late-stage, low-mass star ($\lesssim 1\ M_\odot$), the binary system is called a low-mass X-ray binary (e.g., Frank et al. 2002; Tauris & van den Heuvel 2006). In LMXBs, the neutron star accretes matter via Roche-lobe overflow. Due to the evolved stage of the neutron star companion, the accreted matter consists mainly of hydrogen and helium. If the donor star is a He white dwarf, accretion of predominantly helium is possible as well (e.g., Melia 2009). The infalling matter loses its angular momentum by forming an *accretion disk*. A *boundary layer* marks the point where the accreted matter decelerates from accretion disk to neutron star velocities (e.g., Inogamov & Sunyaev 1999, 2010; for a review, see Popham & Sunyaev 2001). Besides the accretion disk and the boundary layer, the neutron star is surrounded by a *corona*, an optically thin but geometrically thick region of hot electrons (e.g., Thorne & Price 1975; Ibragimov et al. 2005). The formation history of the corona, as well as its shape, is still under debate. The emission of the corona and the accretion disk constitutes the *persistent emission*.

The persistent emission can be detected in the X-ray band. The neutron star and the accretion disk emit approximately as black bodies in the low X-ray energy range (i.e., their photons are *soft*). The neutron

star blackbody emission is diluted due to photon interaction with the neutron star atmosphere (e.g., Calder et al. 2020). Accretion disks are often modeled with a multicolor blackbody (e.g., Bult et al. 2019). For the standard blackbody radiation, a single temperature suffices as a parameter. In contrast, a multicolor blackbody model accounts for the disk temperature varying with distance to the neutron star (Pringle 1981). Repeated Compton up-scattering of soft disk photons gives the coronal emission its power-law shape and places its contribution in the high X-ray energy range (i.e., its photons are *hard*) (e.g., Thorne & Price 1975; White & Holt 1982). Since the total emission depends on the different parts of the neutron star system, it holds key information regarding the properties of the neutron star and its environment.

Observations showed that the neutron star emission varies, depending on its accretion rate. A neutron star with a low accretion rate is in the *hard state*. The hard state emission is dominated by a power-law (e.g., Ibragimov et al. 2005; Burke et al. 2017). In this state, it is believed that the corona occupies the region between the neutron star and a thin truncated accretion disk (e.g., Gierliński & Done 2002; Mayer & Pringle 2007). The *soft state* is marked by a high accretion rate, during which the thermal emission of the accretion disk dominates. The accretion disk reaches till close to the NS, while the corona condenses onto the disk (e.g., Meyer et al. 2000a,b). A neutron star can transition from the soft to the hard state and vice versa.

2.2 Type I X-Ray Bursts

The observed emission fundamentally changes in the event of a type I X-ray burst, which results from unstable nuclear burning of accreted matter. The accreted matter from the donor star accumulates onto the NS, leading to an increase in pressure and temperature at its surface. Eventually, nuclear burning sets in. Due to thin-shell instability and some electron degeneracy (e.g., Schwarzschild & Härm 1965; Galloway & Keek 2021), the neutron star cannot cool by expansion. Thus, its surface heats up further (Galloway & Keek 2021).

The stability of nuclear burning is decided by the heating rate ϵ_{heat} and radiative cooling rate ϵ_{cool}. The heating rate depends on the amount of energy freed by nuclear burning and on compressional heating. The efficiency of nuclear burning varies with temperature and burning process. Hydrogen burns via the CNO cycle, helium through the 3α process, and carbon via carbon fusion. Compressional heating depends on the column depth as well as on the mass accretion rate. A higher accretion rate increases compression and thus the temperature. If $\epsilon_{heat} = \epsilon_{cool}$ and material is accreted at the same rate as it is burnt, the burning is stable. Burning turns unstable once $d\epsilon_{heat}/dT > d\epsilon_{cool}/dT$. In that case, an increase in temperature increases the heating rate more than radiation can cool, which increases the temperature and thus the heating rate even more. The burning rate increases with temperature, leading to more and more material being burnt. This unstable nuclear burning is also called a *thermonuclear runaway* (Keek & Heger 2016). The unstable nuclear burning then encompasses the whole star and burns most of the accumulated matter within seconds (Galloway & Keek 2021).

The burning heats the neutron star, causing an exponential increase in the light curve count rate in the X-ray band, followed by an exponential decay (e.g., Galloway et al. 2008; Keek et al. 2018b; Bult et al. 2019, see also top panel of Fig. 1). During this time span, an X-ray burst radiates $\sim 10^{39}$ ergs of energy (Galloway et al. 2008). While X-ray bursts usually last several seconds, longer and more powerful ones lasting several minutes (*intermediate-duration bursts*) or several hours (*superbursts*) have been observed (e.g., Strohmayer & Brown 2002; Degenaar et al. 2013; Keek et al. 2014, 2017). The difference between these bursts lies in the ignited material. While regular bursts are due to unstable nuclear burning of helium and hydrogen, intermediate duration bursts start with the ignition of a very thick helium layer (in't Zand et al. 2005; Cumming et al. 2006). Superbursts are the product of ignited carbon (Cumming & Bildsten 2001; Strohmayer & Brown 2002; Keek & Heger 2016).

The spectral emission of X-ray bursts is generally modeled as a blackbody, with blackbody temperatures reaching ≈ 3 keV (e.g., Swank et al. 1977; Galloway et al. 2008). However, atmospheric models show that a

diluted blackbody is more appropriate. The source of the dilution, visible as an emission excess at < 3 keV, are the relatively cold electrons in the atmosphere compared to the burst photons, which Compton scatter the burst photons (e.g., Lapidus et al. 1986; London et al. 1986; Suleimanov et al. 2011a).

Since an X-ray burst occurs due to accreted material, subsequent accretion can make bursts a recurrent event. Neutron stars can accrete enough material for a regular burst within hours or days (e.g., Aranzana et al. 2016; Roy et al. 2021). Superbursts need to build a carbon layer, which forms at a greater depth. They therefore have longer recurrence times of months to years (e.g., Kuulkers et al. 2004; Keek et al. 2006). As a contrast, *double bursts* are two bursts separated by only minutes. The short recurrence time implies that the first burst did not burn all the accreted material allowing a second burst to ignite shortly afterwards (e.g., Aranzana et al. 2016; Keek & Heger 2017).

2.2.1 The impact of a Type I X-ray burst on the persistent emission

Initially, the persistent emission was thought to remain constant during the burst. The persistent emission was therefore subtracted from the total one to study the burst emission (e.g., Sztajno et al. 1986; Ji et al. 2013). However, both observations and simulations have shown that this approach is too simplistic.

The X-ray burst increases the mass accretion rate, which increases the amount of persistent emission. The increase in persistent emission can be quantified with a normalization parameter f_a, first introduced by Worpel et al. (2013, 2015). In their method, the persistent emission is fixed in shape, but its amplitude is free to vary by f_a. Worpel et al. (2013, 2015) fitted burst spectra first conventionally (i.e., subtracting the persistent emission first), then again with a varying persistent emission. They found that the parameter f_a improved their fits. For most bursts, $f_a > 1$ and increased with flux. Worpel et al. (2013) interpreted the increase in f_a as increased mass accretion, caused by a stronger Poynting-Robertson (PR) drag. The burst photons increase the PR drag impinging on the infalling matter, causing it to fall towards the neutron star faster (Walker & Meszaros 1989; Ballantyne & Everett 2005; Fragile et al. 2018b, 2020). The mass accretion rate due to PR drag depends on the luminosity (Walker & Meszaros 1989). Hence, the f_a parameter tends to peak at higher values for PRE bursts compared to non-PRE ones (Worpel et al. 2013, 2015).

Changes in the persistent emission are also due to changes in reflection features. In the case of neutron stars in LMXBs, reflection features mostly occur due to radiation reprocessing in the accretion disk (e.g., Cackett et al. 2010). Reprocessing leads to discrete features such as emission lines, most notably an Fe Kα line at $\approx 6 - 7$ keV (e.g., Nandra & Pounds 1994; Fabian et al. 2000; Ballantyne & Ross 2002). The basis of the reflection spectra continuum are processes such as bremsstrahlung, photoionization, or Compton scattering (e.g., Ballantyne 2004). The latter one leads to an often-observed Compton hump > 10 keV (e.g., Lightman & White 1988; George & Fabian 1991; Mondal et al. 2021). Several observations detected emission lines during X-ray bursts, such as an Fe Kα line and lines at ≈ 1 keV (e.g., Strohmayer & Brown 2002; Degenaar et al. 2013; Keek et al. 2014, 2017; Bult et al. 2019). The reprocessing of burst radiation also leads to enhanced emission in the soft X-ray band. This emission is not part of the burst emission and is therefore referred to as *soft excess* (e.g., Keek et al. 2018a; Bult et al. 2019; Sánchez-Fernández et al. 2020). The cause of the soft excess due to reflection (the increase in mass accretion rate increases the soft emission as part of the persistent emission as well) is bremsstrahlung and Compton scattering (Speicher et al. 2022). Since the burst radiation is the dominant source of emission during a burst, the reflection spectrum varies with burst luminosity as shown by Strohmayer & Brown (2002); Keek et al. (2014, 2018a); Speicher et al. (2022).

The X-ray burst not only impacts the accretion disk emission, but the coronal emission as well. The soft burst photons Compton scatter in the corona, causing coronal cooling (e.g., Maccarone & Coppi 2003; Degenaar et al. 2018; Fragile et al. 2018b; Speicher et al. 2020). The cooling reduces the emission at higher energies (e.g., Maccarone & Coppi 2003; Degenaar et al. 2018; Sánchez-Fernández et al. 2020; Speicher et al. 2020).

2.3 Photospheric radius expansion (PRE) bursts

The *Eddington limit* determines the point at which the radiative force equals the force of gravity (e.g., Melia 2009). At the surface of a neutron star with radius R_* and mass M_* the Eddington luminosity is, accounting for general relativity (e.g., Suleimanov et al. 2011b),

$$L_{Edd} = \frac{4\pi c G M_*}{\kappa_{Th}} (1 + z_*) \,, \tag{1}$$

where c is the speed of light and G is the gravitational constant. In the atmosphere, electron scattering is not impacted by relativistic effects due to a relatively low atmospheric temperature of $\sim 10^7$ K. Hence, the electron scattering opacity is the Thomson one $\kappa_{Th} = 0.2(1+X)$ cm^2 g^{-1}, where X is the hydrogen fraction (e.g., Paczynski & Anderson 1986). The gravitational redshift factor $1 + z_*$ is (Lewin et al. 1993),

$$1 + z_* = \left(1 - \frac{2GM_*}{c^2 R_*}\right)^{-1/2} . \tag{2}$$

The Eddington limit varies within the neutron star. At some radial distance r close to the surface, the local Eddington luminosity L_{cr} is (e.g., Paczynski & Anderson 1986)

$$L_{cr} = \frac{4\pi c G M_*}{\kappa_e} (1 + z) \,. \tag{3}$$

The graviational redshift factor $1 + z$ is $\left(1 - \frac{2GM_*}{c^2 r}\right)^{-1/2}$. In this expression, because r is so close to the neutron star radius, the mass not contained within r is negligible (Paczynski & Anderson 1986). When helium ignites, the temperature at the ignition base can exceed 10^9 K, which decreases the opacity κ_e compared to κ_{Th} due to Klein-Nishina corrections, and (e.g., Hanawa & Sugimoto 1982; Ebisuzaki et al. 1983; Kato 1983),

$$\kappa_e = \frac{0.2(1+X)}{1 + 2.2\left(\frac{T}{10^9 \text{ K}}\right)} \text{ cm}^2 \text{ g}^{-1}. \tag{4}$$

The high temperatures at the ignited layers decrease κ_e, which allows the radiation flux to quickly diffuse outward. The decrease in κ_e increases L_{cr}, so that the luminosity may be below the local Eddington limit L_{cr} but above the atmospheric Eddington limit L_{Edd}. In the atmosphere, the radiation encounters a larger scattering opacity. The force due to radiation pressure then lifts the photosphere off during the photosphere radius expansion (e.g., Paczynski & Proszynski 1986). If the luminosity at the base of the expanding envelope as seen from infinity $L_{b,\infty}$ is relatively low, $0.7 L_{Edd} \lesssim L_{b,\infty} \lesssim L_{Edd}$, the photosphere can maintain hydrostatic equilibrium through expansion (Paczynski & Anderson 1986). However, if the luminosity exceeds the Eddington limit, the excess energy causes a radiative wind that removes material from the neutron star (e.g., Ebisuzaki et al. 1983; Kato 1983). The wind can remove ashes of heavy elements with a composition depending on the depth from which the wind is launched (Weinberg et al. 2006). The heavy elements imprint themselves in observations through absorption lines (e.g., in't Zand & Weinberg 2010; Barrière et al. 2015; Kajava et al. 2017).

About 20% of the X-ray bursts exhibit PREs, where the photosphere usually expands by a few factors (Galloway et al. 2008). However, during *superexpansion bursts*, radius expansions by $\gtrsim 10^3$ km are possible (in't Zand & Weinberg 2010). Observationally, the total luminosity is constant during the burst (e.g., Tawara et al. 1984), and is close to the Eddington luminosity (e.g., Keek et al. 2018b). As an example, Kuulkers et al. (2003) determined Eddington luminosities of $\sim 4 \times 10^{38}$ erg s^{-1}. However, this luminosity depends on the neutron star structure and composition (eq. 1, 4). Ignition in helium layers causes high luminosities (e.g., Fujimoto et al. 1987; Woosley et al. 2004), which makes neutron star accreting from He white dwarfs especially prone for exhibiting powerful PREs (e.g., in't Zand & Weinberg 2010). Assuming a blackbody

profile and because $L_{Edd} = 4\pi R^2 \sigma T_{eff}^4$ =constant (e.g., Strohmayer & Bildsten 2003), the observed blackbody temperature decreases during expansion (second and third panel of Fig. 1). With decreasing blackbody temperature, the flux in the X-ray band drops. For superexpansion bursts, the X-ray emission decrease can be so extreme that this phase appears as a separate precursor event (e.g., Hoffman et al. 1978; in't Zand et al. 2012). However, new observatories like *NICER*, sensitive to energies down to 0.2 keV (Gendreau & Arzoumanian 2017), can cover the emission gap in low energies (e.g., Keek et al. 2018b). As the photosphere falls back, the blackbody temperature and thus the flux in the X-ray band increase again. The point where the photosphere falls back onto the neutron star is referred to as *touchdown* (e.g., Damen et al. 1990). The touchdown flux coincides with the maximum blackbody temperature and a minimum blackbody radius. It is equated with the Eddington flux. Özel (2006) argued that the touchdown flux is not smaller because a weaker flux would cause the photosphere to fall back much faster than observed.

2.3.1 Applications of PRE bursts

PRE bursts pose an interesting field of study not only due to their extremeness, but also because they have been used to measure distances as well as the neutron star radii and masses. The neutron star radius and mass can help constrain the nuclear equation of state (e.g. Steiner et al. 2010). The versatility of PRE burst stems from the assumption that the flux at touchdown is the Eddington flux.

Measuring distances with PRE burst has first been proposed by van Paradijs (1978). To establish these bursts as a standard candle, studies tried to find the Eddington luminosity by determining the average burst luminosity (e.g. van Paradijs 1981; Verbunt et al. 1984; Kuulkers et al. 2003). If the maximum measured burst flux $F_{pk,PRE}$ during the PRE were equated with the Eddington flux F_{Edd}, $F_{pk,PRE}$ together with the burst luminosity could yield the distance as (e.g., Galloway et al. 2008),

$$D = \left(\frac{L_{Edd,\infty}}{4\pi F_{pk,PRE}} \right)^{1/2} \tag{5}$$

$L_{Edd,\infty}$ is the Eddington luminosity as seen by a distant observer. An observed luminosity is gravitationally redshifted compared to the luminosity emitted at the star's surface, L_*, via (Lewin et al. 1993),

$$L_\infty = L_*(1+z_*)^{-2}, \tag{6}$$

with a redshift factor depending on the neutron star radius R_* and mass M_* (eq. 2). However, eq. 5 is not conclusive. The Eddington luminosity not only depends on the specific neutron star's dimension and composition. Galloway et al. (2008) also observed different maximum burst fluxes for different bursts of the same source.

Another application of PRE bursts is constraining the mass-radius relationship of neutron stars, either via the *touchdown* or the *cooling tail method*. These methods require two quantities. The first one is the Eddington flux. The observed Eddington flux is (e.g., Özel et al. 2009; Suleimanov et al. 2011b),

$$F_{Edd} = \frac{L_{Edd\infty}}{4\pi D^2} = \frac{GM_* c}{\kappa_{Th} D^2} \frac{1}{1+z_*}. \tag{7}$$

The second quantity is either the blackbody normalization $K = (R_{bb}/D)^2$ or $A = (R_\infty/D)^{-1/2}$. The blackbody radius R_{bb} is related to the actual neutron star star radius as seen from a distance, R_∞, through the color correction factor f_c, via $R_\infty = f_c^2 R_{bb}$, so that (e.g., Suleimanov et al. 2011b,a)

$$K = \left(\frac{R_{bb}}{D} \right)^2 = \frac{1}{f_c^4} \left(\frac{R_\infty}{D} \right)^2 = \frac{1}{f_c^4} A^{-4}. \tag{8}$$

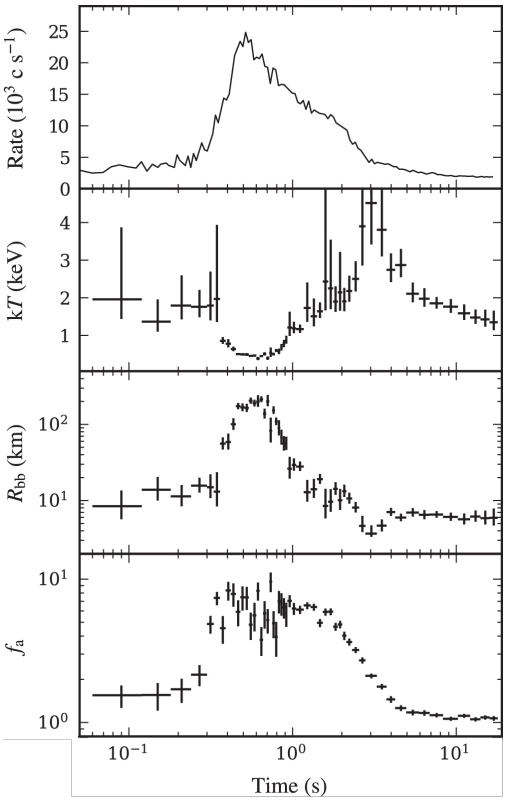

Figure 1: Evolution of spectral parameters during a PRE burst. Top panel: The light curve increases exponentially, followed by an exponential decay over the course of $\sim$ 10 s. Second panel: The blackbody temperature increases prior to the expansion. As the photosphere expands (third panel), the blackbody temperature decreases. The blackbody temperature reaches its maximum at touchdown, coinciding with a minimum of the blackbody radius. The blackbody radius asymptotes to a constant value after touchdown due to a changing color correction factor and potentially a changing emission area due to anisotropies (see section 2.3.1). Bottom panel: During the burst, the normalization constant of the persistent emission increases due to an enhanced accretion rate (section 2.2.1). This figure is adapted from Keek et al. (2018b).

The Eddington flux and the blackbody normalization form a set of equations that allow the determination of the neutron star mass and radius. Following the derivations of Suleimanov et al. (2011b) and defining the compactness $u \equiv 2GM/(R_* c^2)$, rewriting eq. 7 yields

$$R_* = \frac{2\kappa_{Th} D^2 F_{Edd}}{c^3} u^{-1} (1-u)^{-1/2}, \tag{9}$$

while eq. 8 gives

$$R_* = f_c^2 D \sqrt{K} = D A^{-2} \sqrt{1-u}. \tag{10}$$

Eq. 9, 10 are equal if

$$u(1-u) = \frac{2\kappa_{Th} D F_{Edd}}{\sqrt{K} f_c^2 c^3}. \tag{11}$$

Knowing u to solve for R_* also yields M_*, since

$$M_* = \frac{c^2}{2G} u R_*. \tag{12}$$

Eq.11 can yield two solutions for u, from which the most probable $R_* - M_*$ pair is chosen using statistical analysis (e.g., Özel et al. 2009; Güver et al. 2010b; Poutanen et al. 2014; Miller & Lamb 2016). While the Eddington flux and K above also provide a distance constraint (e.g., Özel 2006; Suleimanov et al. 2011b), many studied neutron stars are in globular clusters, to which the distance can be measured independently (e.g., Kuchinski et al. 1995; Valenti et al. 2007).

In the touchdown method, the Eddington flux is equated with the bolometric flux at touchdown (e.g., Özel et al. 2009; Güver et al. 2010a,b). Based on models by for example Madej et al. (2004), it is furthermore assumed that f_c is between 1.3-1.4 (e.g. Özel 2006; Özel et al. 2009; Güver et al. 2010a,b). In an alternative approach, Özel (2006) obtains an additional equation with a redshift measurement through absorption lines. The normalization K is measured in the cooling tail, once the normalization becomes constant (e.g., Özel et al. 2009).

The third panel of Fig. 1 shows that the normalization changes after the touchdown. The driving mechanisms behind the change in normalization are not entirely determined yet. One factor is the color correction factor, which decreases as the luminosity recedes from Eddington lumionsity according to atmosphere models (e.g., Suleimanov et al. 2011a). In addition, Zhang et al. (2013) found a correlation between the dip in normalization and burst oscillations, which some have proposed to be due to cooling wakes. Since the neutron star is not emitting uniformly in the presence of cooling wakes, a changing emitting area could affect the normalization trend as well (Zhang et al. 2013).

The touchdown method suffers from several drawbacks as identified by e.g., Steiner et al. (2010); Suleimanov et al. (2011b); Poutanen et al. (2014); Miller & Lamb (2016). This method assumes that the flux at touchdown is the Eddington flux, at which point the photospheric radius has completely resettled. However, both the touchdown flux corresponding to the Eddington flux and the resettlement of the photospheric radius at touchdown have been disputed (e.g., Steiner et al. 2010; Suleimanov et al. 2011b). Moreover, constraining f_c to 1.3-1.4 in the cooling tail may be unrealistic (e.g., Steiner et al. 2010; Suleimanov et al. 2011b; Poutanen et al. 2014). Determining the blackbody normalization at only one data point is another source of error (e.g., Suleimanov et al. 2011b). In addition to those factors, it can also yield inconsistent or nonphysical results (e.g., Steiner et al. 2010; Poutanen et al. 2014).

An alternative to the touchdown method is the cooling tail method. The cooling tail method does not use the flux at touchdown as the Eddington flux, but rather keeps F_{Edd} and the quantity A as free parameters (e.g., Suleimanov et al. 2011a,b). In the cooling tail, variations in f_c drive changes in the normalization constant K, because after touchdown, R_∞/D becomes constant (eq. 8). The evolution of $K^{-1/4}$ with flux therefore gives insight into changes in f_c. The color correction factor f_c depends on the relative luminosity $L/L_{Edd} = F/F_{Edd}$ and on atmospheric properties, such as composition (e.g., Suleimanov et al. 2011a, 2012; Nättilä et al. 2015). The $K^{-1/4} - F$ relation is used to fit the relation $f_c - (L/L_{Edd} = F/F_{Edd})$ to determine A and F_{Edd} (e.g., Suleimanov et al. 2011b,a). The parameters A and F_{Edd} allow to constrain the neutron star radius and mass, following the same calculations as the touchdown method (e.g., Suleimanov et al. 2011b, , eq. 9-12).

The analysis described above assumes that the burst emission drives the emission evolution. Changes in the persistent emission have been largely ignored. However, observations and analysis show that the burst alters the accretion flow and therefore its emission (section 2.2.1). Neglecting these alterations could therefore introduce errors in the PRE burst analysis. My proposed work intends to study accretion flow changes due to PRE bursts in more detail as outlined in section 4.

3 Previous Work

In my previous work, I studied the impact of Type I X-ray Bursts on the corona and on the reflection spectrum.

In Speicher et al. (2020), we build upon and expand the equations presented in section 5.2.3 in Degenaar

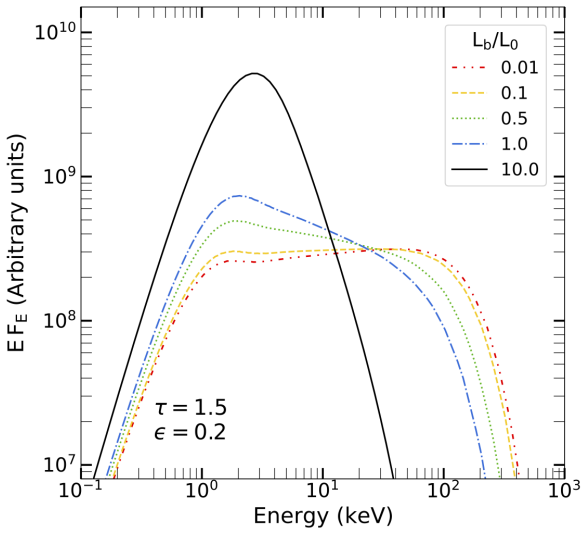

Figure 2: Spectra of a corona with an aspect ratio ϵ, coronal height divided by coronal radius, of 0.2 and an optical depth τ of 1.5 impacted by a Type I X-ray burst of varying burst luminosity L_b/L_0. The increase in burst luminosity cools the corona and leads to a hard X-ray shortage, while the soft X-ray emission increases. This figure is taken from Speicher et al. (2020).

et al. (2018). These equations describe the partition of the accreted energy within a neutron star system consisting of a neutron star, an accretion disk, and a corona. With these equations and the hybrid plasma emission code EQPAIR (Coppi 1999), we study the impact of burst and coronal properties on the coronal emission and its electron temperature.

We show that the soft photons due to the burst can induce significant Compton cooling, and can reduce the coronal electron temperature by a factor of $\gtrsim$ 10. The cooling of the corona causes its hard X-ray emission (in Speicher et al. (2020) defined to be in the 30-50 keV band) to drop down to $\lesssim$ 1 % of its preburst emission (Fig. 2). Coronal cooling is enhanced for a higher coronal aspect ratio and for a higher optical depth. While the aspect ratio, the coronal height divided by the coronal radius, increases the amount of photons intercepting the corona, a greater optical depth leads to more photon-electron interactions and thus more cooling. In the meantime, the soft emission (in Speicher et al. (2020) within the 8-24 keV band) increases due to the additional soft photons (Fig. 2). An increasing mass accretion rate mitigates coronal cooling, because more energy is dissipated in the corona.

In Speicher et al. (2022), we investigated the changes of the reflection spectrum due to a Type I X-ray burst. For this work, we utilize time-averaged two-dimensional density and flux data of six time intervals, spanning from the bursts onset to just past its peak, from the Fragile et al. (2020) simulation. For every time interval, we calculated reflection spectra with the code by Ballantyne et al. (2001) .

Our calculations show that the increasing burst flux ionizes the accretion disk, which weakens any present emission lines (Fig. 3). While the emission lines decrease in strength, the soft excess, the emission < 3 keV not attributed to the burst emission, increases due to increased Compton scattering and bremsstrahlung rates. Our calculations show that reflection produces a soft excess, which may, besides the soft excess due to an increase in mass accretion rate, be a standard feature during X-ray bursts. Moreover, we find that the soft excess is dependent on the accretion disk geometry such as a changing inner accretion disk radius or a changing disk height during the burst. We therefore demonstrate that the soft excess also has the potential

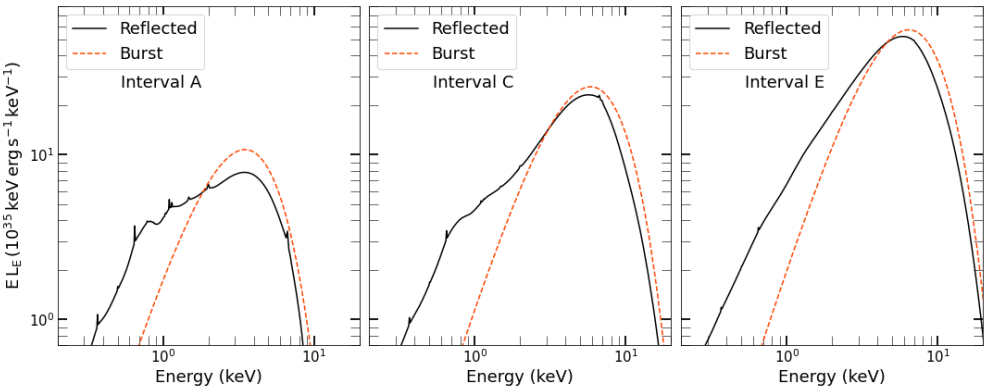

Figure 3: Reflection spectra at different stages of the burst. As the burst (red dashed line) strengthens, it heats and ionizes the accretion disk. The shown stages of the burst are the onset of the burst (A, left panel), midway of the burst rise (C, middle panel), and peak of the burst (E, right panel). The strengthening burst weakens emission lines and increases the soft excess, the emission < 3 keV not attributed to the burst emission. This figure is taken from Speicher et al. (2022).

to give us further insight into the accretion disk geometry.

4 Proposed Work

4.1 Motivation

PRE bursts are a prime-tool for determining the mass-radius relationship of neutron stars and thus for constraining the nuclear equation of state. However, the analysis relies on the assumption that any changes in the emission are due to the burst. As section 2.2.1 showed, the accretion environment changes during the burst, with noticeable effects on the persistent emission. Variations in this emission will affect the derived PRE burst parameters.

The burst flux could be overestimated due to an increase in mass accretion rate and due to reflection. As Bhattacharyya et al. (2018); Roy et al. (2021) showed, analyzing the burst emission with the f_a method (i.e., leaving the normalization constant of the persistent permission as a free parameter, section 2.2.1) leads to a smaller inferred neutron star radius. Reflection in the accretion disk can be another source of error. The reflected emission increases during the burst. The disk will be highly ionized at a high burst flux, which causes the disk to almost mirror the burst emission at the burst peak (Speicher et al. 2022). As a consequence, the burst emission could appear enhanced. The apparently stronger burst flux could lead one to infer a larger F_{Edd}, which in turn impacts the calculated neutron star parameters and distance estimates.

In addition, an evolving shape of the persistent spectrum can introduce fitting uncertainties. The soft excess due to reflection varies during the burst (e.g., Keek et al. 2018a; Speicher et al. 2022). Moreover, Compton cooling of the corona causes a hard X-ray shortage (e.g., Maccarone & Coppi 2003; Sánchez-Fernández et al. 2020; Speicher et al. 2020). Because the persistent emission is assumed to be constant in shape, its evolution could worsen the fits and therefore widen their error bars and make fits less reliable.

While the simulations by Fragile et al. (2018b, 2020) showed the evolution of the accretion flow due to a regular Type I X-ray burst, the impact of a photospheric radius expansion has not been evaluated yet. While the accretion flow interaction with a regular versus a PRE burst may share similarities, such as heating of the accretion disk as shown by Fragile et al. (2020), new effects could surface. The ejection of material due to wind or the PRE itself could perturb the accretion flow. The perturbation could affect the accretion rate. If

this perturbation removed some angular momentum from the accreting matter, it might fall in faster towards the neutron star. Alternatively, the wind could push the accretion flow further away, increasing its time to reach the neutron star. The speed of the expansion of the photosphere could also decide over geometric changes in the accretion flow. Suppose the increase in mass accretion rate during the PRE burst can deplete the inner accretion flow region at least as fast as the photosphere expands. In that case, significant geometrical changes may be avoided. However, if the expansion were too fast, the accretion flow could ”pile up” onto the photosphere. The PRE could thus significantly impact the accretion flow, which could fundamentally alter the persistent emission.

Due to the significance of PRE bursts and the still unaccounted for potential effects the evolving accretion flow might have, I propose to study the accretion flow subject to a PRE burst through simulations. For the simulations, I intend to use the hydrodynamics code *Cosmos*++, since it already successfully displayed the capacity to simulate accretion flows impacted by regular Type I X-ray bursts (Fragile et al. 2018b, 2020). For the proposed simulations, I need to advance *Cosmos*++ in steps as described in sections 4.3-4.5. To succeed with the proposed implementations, Dr. Ballantyne and I will collaborate with Dr. Fragile.

4.2 Simulations

The simulation code I will use is the astrophysics code *Cosmos*++ (Anninos et al. 2005; Fragile et al. 2012, 2014). *Cosmos*++ numerically evolves the equations of viscous radiation hydrodynamics, which describe the conservation of energy and the components of momentum for radiation and fluid fields. While *Cosmos*++ offers a variety of time integration methods, such as 2nd order Euler, 2nd order Runge–Kutta, 2nd order Crank–Nicholson, and 3rd order Euler (Fragile et al. 2012), Fragile et al. (2014) implemented an explicit-implicit evolution scheme to improve the handling of the radiation in the code.

I will use this code due to several advantages, starting with the simulation space. The simulation mesh is multidimensional, which allows tracing the evolving structure of the accretion flow. The mesh cell structure of *Cosmos*++ is also customizable (Anninos et al. 2005). Fragile et al. (2018b, 2020) use this feature to enhance the simulation resolution towards the midplane and thus the accretion flow (see also section 4.4).

Cosmos++ is capable of capturing the dominating physics of the neutron star environment. Close to the neutron star, relativistic effects have to be taken into account. Thus, the code’s applicability to not only Newtonian but also general-relativistic problems will be highly beneficial (Anninos et al. 2005). Fragile et al. (2018b, 2020) for instance use the Kerr metric in their simulations. *Cosmos*++ also implements relevant physical processes. The code currently includes free-free absorption/emission, Thomson scattering, and Compton heating/cooling. While the electron-scattering opacity is assumed to be constant in Fragile et al. (2018b, 2020), the code offers the possibility to switch to a temperature-dependent one. Any switches or modifications in the code will be achievable since we will collaborate with Dr. Fragile from the College of Charleston, who is one of the developers of *Cosmos*++. The code also has the option to treat magnetic fields (e.g., Fragile et al. 2012). However, for our problem setup their effects will be negligible enough to ignore them. The magnetic field of neutron stars in LMXB is generally weak. The magnetic field field decays over time due to rotation and, in the case of LMXB, also likely due to accretion (Taam & van den Heuvel 1986; Cumming et al. 2001). This will not only simplify the applied code, but also the physical scenario and will allow to focus on the impact of solely the X-ray burst.

Moreover, the implementation of *Cosmos*++ has been tested. Its ability to capture shocks correctly has been tested with four shock tube tests involving non-relativistic and midly relativistic shocks, as well as highly and radiation-pressure dominated, mildly relativistic waves (Fragile et al. 2012, 2014). *Cosmos*++ has also been tested to simulate accretion flows around black holes and neutron stars (Fragile et al. 2012, 2014, 2018a,b, 2020).

4.3 Enhancing current simulations with a neutron star spin

In the simulations by Fragile et al. (2018b, 2020), the neutron star does not rotate. However, a nonzero spin is not the most realistic scenario. In fact, many neutron stars spin with a frequency of ~ 500 Hz (e.g., Patruno et al. 2017), so that relativistic effects could become important. Besides being more realistic, a neutron star spin will impact its surroundings. PR drag, and thus the amount of disk depletion during the X-ray burst, depends on the neutron star spin (Walker & Meszaros 1989). In addition, the neutron star spin affects the innermost stable circular orbit accreting matter can have (e.g., Pachón et al. 2006; Török et al. 2014). A prograde spin will thus move the accretion disk closer to the neutron star. Since a neutron star spin is both realistic and relevant for the accretion flow, I intend to enhance the existing simulations with a neutron star spin as a first step.

Adding the neutron star spin will require a modification of the radiation field leaving the neutron star. The current code is already capable of propagating the radiation through the simulation space, so I will only need to change the radiation crossing the simulation boundary. Without a spin, the neutron star emits radially. If the simulation setup includes a spin, the direction of radiation will also have some angle dependence out of an observer's point of view. To implement changes of the radiation field, I will need to adjust its time components of the stress-energy tensor.

The radiation leaving a spinning neutron star has already been studied by for example Bakala et al. (2019). In their work, they study PR drag for a rotating neutron star. For this purpose, they describe the emitted radiation, including its stress-energy tensor, in the Kerr spacetime geometry. As they not only account for relativistic effects but also use the same metric as the simulation, their equations are highly applicable to our problem.

Adding the neutron star spin will yield two new problem setups, for accretion flows in the hard and in the soft state respectively (see sections 4.4,4.5). Comparisons of the simulations with spin with those by Fragile et al. (2018b, 2020) will determine the impact of the spin on the response of the accretion flow. Moreover, variations in the spin will show the influence of the spin magnitude.

4.4 Implementing a PRE burst impacting the accretion flow in the hard state

As already mentioned in section 2.1, in the hard state, when the accretion rate is low, a thick accretion flow in the form of a corona settles between the neutron star and a thin truncated accretion disk (e.g., Gierliński & Done 2002; Mayer & Pringle 2007). Fragile et al. (2018b) simulated the corona impacted by a regular Type I X-ray burst. In their simulation, the burst enhances PR drag and thus the mass accretion rate. In addition, the soft burst photons cool the coronal through Compton scattering. Bereft of the thermal pressure support, the corona collapses. Both the cooling while expanding photosphere and the ejected ashes may intensify coronal cooling. The mass accretion rate could increase due to photosphere-corona interaction during the PRE or decrease due to the neutron star's spin. To investigate the actual behavior of the thick accretion flow, I will base my simulation on those by Fragile et al. (2018b).

In their setup, the corona is initialized as a hydrodynamic torus as described by Kozlowski et al. (1978). This type of torus falls under the category of *Polish doughnuts*, and are often used to simulate thick accretion flows (e.g., Zanotti et al. 2003; Antón et al. 2006; Porth et al. 2019). These tori follow the *von Zeipel theorems*, which are a collection of integrability conditions. One condition, for example, is that the angular momentum density only depends on the angular velocity (Abramowicz & Fragile 2013). The torus solution used by Fragile et al. (2018b) assumes that the angular momentum density is constant. The other quantities needed to initialize the torus are its inner radius and the radius at its center, which Fragile et al. (2018b) set at 47 km and 86 km respectively. The height of this torus depends on the sound speed c_s and on the azimuthal gas velocity (Fragile et al. 2018b). The background is filled with a cold, low-density, static gas (Fragile et al. 2018a). I will adjust the two mentioned radii to incorporate the spin dependence of the innermost

stable circular orbit. The accretion flow has a viscosity parameterized with the *Shakura-Sunyaev viscosity parameter* α from the disk solution by Shakura & Sunyaev (1973) (see also section 4.5). In the simulations by Fragile et al. (2018b), $\alpha = 0.025$.

The simulation mesh used by (Fragile et al. 2018b) is two-dimensional and axissymmetric. The mesh resolution increases towards the midplane. The simulation mesh is constrained by an inner radial boundary at $r_{min} = 10.7$ km and an outer radial boundary at $r_{max} = 1531$ km. The neutron star of mass $1.45 M_{\odot}$ is not simulated itself. Instead, the burst flux is injected through the inner radial boundary. In the nonspinning case explored by Fragile et al. (2018b), the burst flux is injected only in the radial direction. The radial component of the burst flux vector is thus the only nonzero one and depends on the burst luminosity L via $F_r = L/(4\pi r_{min}^2)$. In Fragile et al. (2018b), the burst luminosity follows a Gamma-ray burst profile by Norris et al. (2005),

$$L(t) = L_0 e^{2(\tau_1/\tau_2)^{1/2}} e^{\frac{-\tau_1}{t-t_s} - \frac{t-t_s}{\tau_2}}, \tag{13}$$

where $L_0 = 10^{38}$ erg s^{-1}, $\tau_1 = 6$ s, $\tau_2 = 1$ s, and $t_s = -0.4$ s. The radiation interacts with the accretion flow via Kramer-type, grey opacities (Fragile et al. 2018a). For comparing my work to the simulations by Fragile et al. (2018b) and Fragile et al. (2020), I will use the same luminosity profile but I will vary L_0 to reach PRE burst conditions. Also, regarding comparison to observations it may be beneficial to also implement a luminosity profile used to describe type I X-ray bursts (e.g., by Barrière et al. 2015; Pike et al. 2021).

The hydrodynamics of the PRE driven wind will be calculated self-consistently based on the nuclear energy released below the atmosphere (Yu & Weinberg 2018; Herrera et al. 2020). The properties of the PRE will depend on its ignition depth, (e.g., Yu & Weinberg 2018) which I will vary.

The simulations will provide me with two-dimensional, time-dependent information of density, pressure and velocity of the corona. From this, changes in coronal properties including temperature, shape, density and mass accretion rate can be calculated. I will use the variations in coronal properties to predict observational consequences and compare them to observational data.

4.5 Implementing a PRE burst impacting the accretion flow in the soft state

The highly accreting neutron star systems are in the soft state. As already described in section 2.1, the corona condenses onto a thin accretion disk in the high accretion rate regime. When Fragile et al. (2020) simulated the accretion disk impacted by a regular burst, enhanced PR-drag increased the mass accretion rate. The increased mass accretion rate depleted the inner accretion disk region, causing the inner accretion disk radius to retract. The burst also heated the disk. Because the disk is supported by radiation-pressure, the heating expanded the disk height and decreased the disk density and optical depth. A PRE could mitigate heating due to the cooling photosphere and could drive the disk out further due to a greater accretion rate.

To determine the impact of the PRE, I will start with the thin accretion disk simulation by Fragile et al. (2020). Their thin disk setup follows the Shakura-Sunyaev thin disk solution. For thin disks, the height H is much smaller compared to the disk radius. Thus, many properties, such as the mass accretion rate depend on the vertically integrated surface density rather than the height dependent one. The height dependent density can be approximated in the thin disk regime and stems from the vertical hydrostatic equilibrium condition (Fragile et al. 2020),

$$\rho(r, z) = \rho_0 \, e^{-z^2/H^2}. \tag{14}$$

The Shakura-Sunyaev disk solution solves general relativistic equations describing the conservation of mass, radial momentum, angular momentum, and energy as well as describing the vertical equilibrium. The solution factors in spin (Abramowicz & Fragile 2013), so I will not need to introduce new machinery. The Shakura-Sunyaev disk solution is advantageous, because it does not require extensive knowledge about the viscosities due to magnetic fields or turbulence. Instead, the viscosity is parameterized with α, with $\alpha \lesssim 1$. The viscosity is related to α through the disk height H and the speed of sound c_s, $\nu = \alpha c_s H$ (Novikov &

Thorne 1973). Fragile et al. (2020) test two different values for the viscosity parameter α, 0.025 and and 0.1.

The burst luminosity profile (eq. 13), cold, low-density gas in the simulation background and equations describing the radiation propagation are the same as used by Fragile et al. (2018b) (see section 4.4). While the structure of the simulation mesh is the same as for Fragile et al. (2018b), the outer radial boundary occurs at $r_{max} = 352$ km. For eq. 13, Fragile et al. (2020) test $L_0 = 10^{38}$ erg s^{-1} and $L_0 = 3 \times 10^{38}$ erg s^{-1}. Since only the latter L_0 exceeds the Eddington luminosity, I will use its simulation to compare to. As already mentioned in section 4.4, it may be worth exploring a different burst profile and vary L_0 as well.

The simulations will provide me with the same output as described in section 4.4. With this output, I can compute reflection spectra following Speicher et al. (2022). Due to the high burst luminosity, I expect a high degree of ionization of the disk and thus weak emission lines. Regions closer to the neutron star may be less ionized as during regular X-ray bursts due to the cooling photosphere.

4.6 Proposed Timeline

I will start with implementing the neutron star spin (section 4.3). Because simulations of the hard state are computationally cheaper to implement than simulations of the soft state (e.g., Abramowicz & Fragile 2013), I will carry out the simulations described in section 4.4 before those mentioned in section 4.5.

I will begin with incorporating the neutron star spin at the beginning of 2022. I intend to work on the hard state simulations in the academic year 2022-2023 and on the soft state simulations in the following academic year 2023-2024.

For code development and simulations, I will use the PACE system. In addition, due to our collaboration with Dr. Fragile we will be able to run some tasks on the Stampede2 cluster if needed. To convert the simulation data for the soft state (section 4.5) into reflection spectra, we intend to work with undergraduate students.

5 Conclusion

PRE bursts offer a way to probe neutron star properties. However, the burst emission is intertwined with the emission of the accretion flow. Not accounting for burst induced changes in the persistent emission will introduce biases. While observations and simulations have revealed several ways of burst-accretion flow interaction such as coronal cooling, a PRE could introduce additional effects. As PRE bursts are a prime tool for determining the mass-radius relationship of neutron stars, an accurate estimation of PRE burst emissions is of paramount importance. Our simulations will either expose significant alterations of the persistent emission or confirm the correctness of the status quo of PRE burst analysis method and previous studies. Our work will therefore contribute to our understanding of neutron stars and, with the nuclear equation of state, of one of the densest environments in the universe.

References

Abramowicz M. A., Fragile P. C., 2013, Living Reviews in Relativity, 16, 1

Anninos P., Fragile P. C., Salmonson J. D., 2005, ApJ, 635, 723

Antón L., Zanotti O., Miralles J. A., Martí J. M., Ibáñez J. M., Font J. A., Pons J. A., 2006, ApJ, 637, 296

Aranzana E., Sánchez-Fernández C., Kuulkers E., 2016, A&A, 586, A142

Bakala P., De Falco V., Battista E., Goluchová K., Lančová D., Falanga M., Stella L., 2019, Phys. Rev. D, 100, 104053

Ballantyne D. R., 2004, MNRAS, 351, 57

Ballantyne D. R., Everett J. E., 2005, ApJ, 626, 364

Ballantyne D. R., Ross R. R., 2002, MNRAS, 332, 777

Ballantyne D. R., Ross R. R., Fabian A. C., 2001, MNRAS, 327, 10

Barrière N. M., et al., 2015, ApJ, 799, 123

Bhattacharyya S., et al., 2018, ApJ, 860, 88

Bult P., et al., 2019, ApJ, 885, L1

Burke M. J., Gilfanov M., Sunyaev R., 2017, MNRAS, 466, 194

Cackett E. M., et al., 2010, ApJ, 720, 205

Calder A. C., Karpov P. I., Medin Z., Lattimer J. M., 2020, in Journal of Physics Conference Series. p. 012003, doi:10.1088/1742-6596/1623/1/012003

Coppi P. S., 1999, in Poutanen J., Svensson R., eds, Astronomical Society of the Pacific Conference Series Vol. 161, High Energy Processes in Accreting Black Holes. p. 375 (arXiv:astro-ph/9903158)

Cumming A., Bildsten L., 2001, ApJ, 559, L127

Cumming A., Zweibel E., Bildsten L., 2001, ApJ, 557, 958

Cumming A., Macbeth J., in 't Zand J. J. M., Page D., 2006, ApJ, 646, 429

Damen E., Magnier E., Lewin W. H. G., Tan J., Penninx W., van Paradijs J., 1990, A&A, 237, 103

Degenaar N., Miller J. M., Wijnands R., Altamirano D., Fabian A. C., 2013, ApJ, 767, L37

Degenaar N., et al., 2018, Space Sci. Rev., 214, 15

Ebisuzaki T., Hanawa T., Sugimoto D., 1983, PASJ, 35, 17

Fabian A. C., Iwasawa K., Reynolds C. S., Young A. J., 2000, PASP, 112, 1145

Fragile P. C., Gillespie A., Monahan T., Rodriguez M., Anninos P., 2012, ApJS, 201, 9

Fragile P. C., Olejar A., Anninos P., 2014, ApJ, 796, 22

Fragile P. C., Etheridge S. M., Anninos P., Mishra B., Kluźniak W., 2018a, ApJ, 857, 1

Fragile P. C., Ballantyne D. R., Maccarone T. J., Witry J. W. L., 2018b, ApJ, 867, L28

Fragile P. C., Ballantyne D. R., Blankenship A., 2020, Nature Astronomy, 4, 541

Frank J., King A., Raine D. J., 2002, Accretion Power in Astrophysics: Third Edition. Cambridge University Press

Fujimoto M. Y., Sztajno M., Lewin W. H. G., van Paradijs J., 1987, ApJ, 319, 902

Galloway D. K., Keek L., 2021, in Belloni T. M., Méndez M., Zhang C., eds, Astrophysics and Space Science Library Vol. 461, Astrophysics and Space Science Library. pp 209–262 (arXiv:1712.06227), doi:10.1007/978-3-662-62110-3_5

Galloway D. K., Muno M. P., Hartman J. M., Psaltis D., Chakrabarty D., 2008, ApJS, 179, 360

Gendreau K., Arzoumanian Z., 2017, Nature Astronomy, 1, 895

George I. M., Fabian A. C., 1991, MNRAS, 249, 352

Gierliński M., Done C., 2002, MNRAS, 337, 1373

Grimm H. J., Gilfanov M., Sunyaev R., 2002, A&A, 391, 923

Güver T., Özel F., Cabrera-Lavers A., Wroblewski P., 2010a, ApJ, 712, 964

Güver T., Wroblewski P., Camarota L., Özel F., 2010b, ApJ, 719, 1807

Hanawa T., Sugimoto D., 1982, PASJ, 34, 1

Herrera Y., Sala G., José J., 2020, A&A, 638, A107

Hoffman J. A., Lewin W. H. G., Doty J., Jernigan J. G., Haney M., Richardson J. A., 1978, ApJ, 221, L57

Ibragimov A., Poutanen J., Gilfanov M., Zdziarski A. A., Shrader C. R., 2005, MNRAS, 362, 1435

Inogamov N. A., Sunyaev R. A., 1999, Astronomy Letters, 25, 269

Inogamov N. A., Sunyaev R. A., 2010, Astronomy Letters, 36, 848

Ji L., et al., 2013, MNRAS, 432, 2773

Kajava J. J. E., Nättilä J., Poutanen J., Cumming A., Suleimanov V., Kuulkers E., 2017, MNRAS, 464, L6

Kato M., 1983, PASJ, 35, 33

Keek L., Heger A., 2016, MNRAS, 456, L11

Keek L., Heger A., 2017, ApJ, 842, 113

Keek L., in't Zand J. J. M., Cumming A., 2006, A&A, 455, 1031

Keek L., Ballantyne D. R., Kuulkers E., Strohmayer T. E., 2014, ApJ, 789, 121

Keek L., Iwakiri W., Serino M., Ballantyne D. R., in't Zand J. J. M., Strohmayer T. E., 2017, ApJ, 836, 111

Keek L., et al., 2018a, ApJ, 855, L4

Keek L., et al., 2018b, ApJ, 856, L37

Kozlowski M., Jaroszynski M., Abramowicz M. A., 1978, A&A, 63, 209

Kuchinski L. E., Frogel J. A., Terndrup D. M., Persson S. E., 1995, AJ, 109, 1131

Kuranov A. G., Postnov K. A., 2006, Astronomy Letters, 32, 393

Kuulkers E., den Hartog P. R., in't Zand J. J. M., Verbunt F. W. M., Harris W. E., Cocchi M., 2003, A&A, 399, 663

Kuulkers E., in't Zand J., Homan J., van Straaten S., Altamirano D., van der Klis M., 2004, in Kaaret P., Lamb F. K., Swank J. H., eds, American Institute of Physics Conference Series Vol. 714, X-ray Timing 2003: Rossi and Beyond. pp 257–260 (arXiv:astro-ph/0402076), doi:10.1063/1.1781037

Lapidus I. I., Syunyaev R. A., Titarchuk L. G., 1986, Soviet Astronomy Letters, 12, 383

LeBlanc F., 2010, An Introduction to Stellar Astrophysics. Wiley

Lewin W. H. G., van Paradijs J., Taam R. E., 1993, Space Sci. Rev., 62, 223

Lightman A. P., White T. R., 1988, ApJ, 335, 57

London R. A., Taam R. E., Howard W. M., 1986, ApJ, 306, 170

Maccarone T. J., Coppi P. S., 2003, A&A, 399, 1151

Madej J., Joss P. C., Różańska A., 2004, ApJ, 602, 904

Mayer M., Pringle J. E., 2007, MNRAS, 376, 435

Melia F., 2009, High-Energy Astrophysics. Princeton University Press

Meyer F., Liu B. F., Meyer-Hofmeister E., 2000a, A&A, 354, L67

Meyer F., Liu B. F., Meyer-Hofmeister E., 2000b, A&A, 361, 175

Miller M. C., Lamb F. K., 2016, European Physical Journal A, 52, 63

Mondal A. S., Raychaudhuri B., Dewangan G. C., 2021, MNRAS, 504, 1331

Nandra K., Pounds K. A., 1994, MNRAS, 268, 405

Nättilä J., Suleimanov V. F., Kajava J. J. E., Poutanen J., 2015, A&A, 581, A83

Norris J. P., Bonnell J. T., Kazanas D., Scargle J. D., Hakkila J., Giblin T. W., 2005, ApJ, 627, 324

Novikov I. D., Thorne K. S., 1973, in Black Holes (Les Astres Occlus). pp 343–450

Özel F., 2006, Nature, 441, 1115

Özel F., Güver T., Psaltis D., 2009, ApJ, 693, 1775

Pachón L. A., Rueda J. A., Sanabria-Gómez J. D., 2006, Phys. Rev. D, 73, 104038

Paczynski B., Anderson N., 1986, ApJ, 302, 1

Paczynski B., Proszynski M., 1986, ApJ, 302, 519

Patruno A., Haskell B., Andersson N., 2017, ApJ, 850, 106

Pike S. N., et al., 2021, ApJ, 918, 9

Popham R., Sunyaev R., 2001, ApJ, 547, 355

Porth O., et al., 2019, ApJS, 243, 26

Poutanen J., Nättilä J., Kajava J. J. E., Latvala O.-M., Galloway D. K., Kuulkers E., Suleimanov V. F., 2014, MNRAS, 442, 3777

Pringle J. E., 1981, ARA&A, 19, 137

Roy P., Beri A., Bhattacharyya S., 2021, MNRAS, 508, 2123

Sánchez-Fernández C., Kajava J. J. E., Poutanen J., Kuulkers E., Suleimanov V. F., 2020, A&A, 634, A58

Sartore N., Ripamonti E., Treves A., Turolla R., 2010, A&A, 510, A23

Schwarzschild M., Härm R., 1965, ApJ, 142, 855

Shakura N. I., Sunyaev R. A., 1973, A&A, 500, 33

Speicher J., Ballantyne D. R., Malzac J., 2020, MNRAS, 499, 4479

Speicher J., Ballantyne D. R., Fragile P. C., 2022, MNRAS, 509, 1736

Steiner A. W., Lattimer J. M., Brown E. F., 2010, ApJ, 722, 33

Strohmayer T., Bildsten L., 2003, arXiv e-prints, pp astro–ph/0301544

Strohmayer T. E., Brown E. F., 2002, ApJ, 566, 1045

Suleimanov V., Poutanen J., Werner K., 2011a, A&A, 527, A139

Suleimanov V., Poutanen J., Revnivtsev M., Werner K., 2011b, ApJ, 742, 122

Suleimanov V., Poutanen J., Werner K., 2012, A&A, 545, A120

Swank J. H., Becker R. H., Boldt E. A., Holt S. S., Pravdo S. H., Serlemitsos P. J., 1977, ApJ, 212, L73

Sztajno M., van Paradijs J., Lewin W. H. G., Langmeier A., Trumper J., Pietsch W., 1986, MNRAS, 222, 499

Taam R. E., van den Heuvel E. P. J., 1986, ApJ, 305, 235

Tauris T. M., van den Heuvel E. P. J., 2006, Formation and evolution of compact stellar X-ray sources. Cambridge University Press, pp 623–665

Tawara Y., et al., 1984, ApJ, 276, L41

Thorne K. S., Price R. H., 1975, ApJ, 195, L101

Török G., Urbanec M., Adámek K., Urbancová G., 2014, A&A, 564, L5

Valenti E., Ferraro F. R., Origlia L., 2007, AJ, 133, 1287

Verbunt F., van Paradijs J., Elson R., 1984, MNRAS, 210, 899

Walker M. A., Meszaros P., 1989, ApJ, 346, 844

Weinberg N. N., Bildsten L., Schatz H., 2006, ApJ, 639, 1018

White N. E., Holt S. S., 1982, ApJ, 257, 318

Woosley S. E., et al., 2004, ApJS, 151, 75

Worpel H., Galloway D. K., Price D. J., 2013, ApJ, 772, 94

Worpel H., Galloway D. K., Price D. J., 2015, ApJ, 801, 60

Yu H., Weinberg N. N., 2018, ApJ, 863, 53

Zanotti O., Rezzolla L., Font J. A., 2003, MNRAS, 341, 832

Zhang G., Méndez M., Belloni T. M., Homan J., 2013, MNRAS, 436, 2276

in't Zand J. J. M., Weinberg N. N., 2010, A&A, 520, A81

in't Zand J. J. M., Cumming A., van der Sluys M. V., Verbunt F., Pols O. R., 2005, A&A, 441, 675

in't Zand J. J. M., Homan J., Keek L., Palmer D. M., 2012, A&A, 547, A47

van Paradijs J., 1978, Nature, 274, 650

van Paradijs J., 1981, A&A, 101, 174